

CARMA CO($J = 2-1$) OBSERVATIONS OF THE CIRCUMSTELLAR ENVELOPE OF BETELGEUSE

EAMON O’GORMAN¹, GRAHAM M. HARPER¹, JOANNA M. BROWN², ALEXANDER BROWN³, SETH REDFIELD⁴, AND MIGUEL A. REQUENA-TORRES⁵

Draft version January 16, 2012

ABSTRACT

We report radio interferometric observations of the $^{12}\text{C}^{16}\text{O}$ 1.3 mm $J=2-1$ emission line in the circumstellar envelope of the M supergiant α Ori. Observations were made with the Combined Array for Research in Millimeter-wave Astronomy (CARMA) interferometer in the C, D, and E antenna configurations. We obtain excellent uv-coverage (5 - 280 k λ) by combining data from all three configurations allowing us to trace spatial scales as small as 0.9'' over a 32'' field of view. The high spatial resolution C configuration maps show that the inner S1 shell has asymmetric outflow velocities ranging from -9.0 km s⁻¹ to +10.6 km s⁻¹ with respect to the stellar rest frame. We find little evidence for the outer S2 shell in this configuration probably because the majority of this emission has been spatially-filtered (resolved out) by the array. The S2 shell appears as an extra blueshifted emission component in the D and E configuration maps between -11.0 km s⁻¹ and -16.0 km s⁻¹ and we detect it between +10.6 km s⁻¹ and +13.2 km s⁻¹ in the redshifted portion of the line profile. The S2 shell’s outflow velocity is found to be in good agreement with high resolution optical spectroscopy of KI. A discrete off-source emission feature is detected at 5'' S-W of α Ori in all D configuration maps. We image both shells in the multi-configuration maps (all configurations) and see the formation of the classical ring structure for the S2 shell as we sample the line across velocities. We assign an outer radius of 5'' to S1 and propose that S2 extends beyond CARMA’s field of view (32'' at 1.3 mm) out to a radius of 17'' which is larger than recent single dish observations have indicated.

Keywords: circumstellar matter — Stars: individual: (α Ori) — Stars: late-type — Stars: massive — supergiants — Radio lines: stars

1. INTRODUCTION

The circumstellar envelope (CSE) of Betelgeuse (α Ori-*onis* [M2 Iab]) is a proving ground for ideas and theories of mass loss from oxygen-rich M supergiants. Currently it is losing mass at a respectable rate $\sim 3 \times 10^{-6} M_{\odot} \text{ yr}^{-1}$ (Glassgold & Huggins 1986; Huggins et al. 1994; Harper et al. 2001), as it has been in the past ~ 1000 yr. Most of the optically thin silicate dust lies beyond ~ 30 stellar radii (Danchi et al. 1994) and dust is, therefore, unlikely to be responsible for the bulk mass loss as is the case in M-type supergiants. This raises the important point that if the mass loss from Betelgeuse is not a result of dust then perhaps the same mechanisms that are responsible might also be active in the more dusty later M-type supergiants.

Hartmann & Avrett (1984) constructed a magnetic WKB Alfvén wave-driven model for Betelgeuse’s chromosphere and wind that reproduced reasonably well the observed chromospheric emission fluxes and mass loss rate. However, multi-wavelength centimeter continuum radio

observations made with the Very Large Array (VLA) by Lim et al. (1998) revealed that the atmosphere was much cooler than the Alfvén wave-driven model predicted (Harper et al. 2001). Although new nonlinear Alfvén wave models have been computed by Airapetian et al. (2000) there are currently no theoretical models that make specific predictions for *both* the dynamic and thermodynamic state of the mass outflow.

Radiation pressure on atoms and molecules is another potential contributing candidate for mass loss mechanism and so spatial and dynamical studies of molecules are a fruitful line of investigation, especially in relation to eventual formation of dust. The study of CO molecules in the CSE of Betelgeuse began with the detection of 4.6 μm ro-vibrational absorption lines of $^{12}\text{C}^{16}\text{O}$ and $^{13}\text{C}^{16}\text{O}$ by Bernat et al. (1979) who identified two absorption features; one with a Doppler shift of 9 km s⁻¹ towards us with $T_{\text{exc}} \simeq 200$ K, $v_{\text{turb}} \simeq 4$ km s⁻¹ and $N_{12\text{C}^{16}\text{O}} = 4.7 \times 10^{17} \text{ cm}^{-2}$, known as S1, and a faster 16 km s⁻¹ feature with $T_{\text{exc}} \simeq 70$ K, $v_{\text{turb}} \simeq 1$ km s⁻¹ and $N_{12\text{C}^{16}\text{O}} = 1.2 \times 10^{16} \text{ cm}^{-2}$, known as S2. The S1 feature with its higher column density was well known from atomic absorption line studies (e.g. Weymann 1962) and both features had been detected in high spectral resolution atomic Na and K absorption profiles (Goldberg et al. 1975). $^{12}\text{C}^{16}\text{O}$ was subsequently detected at 230 GHz in the $J = 2-1$ rotation emission line by Knapp et al. (1980), although a search for SiO($J = 2-1$) by Lambert & Vanden Bout (1978) had been unsuccessful. The weaker $^{12}\text{C}^{16}\text{O}(J = 1-0)$ line was tentatively detected by Knapp & Morris (1985) with a 7 m dish which had a half-power beamwidth (HPBW) of

¹ Astrophysics Research Group, School of Physics, Trinity College Dublin, Dublin 2, Ireland.

² Harvard-Smithsonian Center for Astrophysics, 60 Garden Street, MS-78, Cambridge, MA 02138, USA.

³ Center for Astrophysics and Space Astronomy, University of Colorado, 389 UCB, Boulder, CO 80309, USA

⁴ Astronomy Department, Van Vleck Observatory, Wesleyan University, Middletown, CT 06459, USA

⁵ Max-Planck-Institut für Radioastronomie, Auf dem Hgel 69, 53121 Bonn, Germany

Table 1
CARMA Observations

Observation Date	Configuration	Time on Source (hr)	Flux Calibrator	Phase Calibrators	Image Cube ^a Dynamic Range ^b
2007 Jun 18	D	0.9	0530+135	0530+135, 0532+075	22.8
2007 Jun 21	D	3.0	0530+135	0530+135, 0532+075	22.7
2007 Jun 24	D	2.1	0530+135	0530+135, 0532+075	26.1
2007 Jun 25	D	2.4	0530+135	0530+135, 0532+075	30.2
2009 Jul 07	E	3.2	3C120	3C120, 0532+075	30.1
2009 Nov 05	C	1.2	3C120	3C120, 0532+075	17.3
2009 Nov 09	C	3.0	3C120	3C120, 0532+075	27.2
2009 Nov 15	C	1.0	3C120	3C120, 0532+075	17.8
2009 Nov 16	C	3.2	3C120	3C120, 0532+075	32.0
All	C	8.4	43.8
All	D	8.4	31.9
All	Multi-configuration	20.0	52.3

^a Low spectral resolution (i.e. channel width of 1.3 km s^{-1}).

^b The peak emission of the image cube divided by the root mean square of the residual image.

100".

Huggins (1987) presented a higher signal-to-noise $^{12}\text{C}^{16}\text{O}(J = 2-1)$ observation of Betelgeuse's CSE with a HPBW of $32''$ and found some evidence for an S2 shell radius of about $16''$ by comparing the $(2-1)/(1-0)$ intensities. However, Huggins et al. (1994) present a 30 m Institut de Radioastronomie Millimétrique (IRAM) $J = 2-1$ profile observed with a smaller $12''$ HPBW that looks remarkably similar, not showing the horned signature expected if it had been resolved, apparently in conflict with the previous S2 shell radius estimate.

Here we present the results of an interferometric study of the rotational $^{12}\text{C}^{16}\text{O}(J = 2-1)$ emission line made with three Combined Array for Research in Millimeter-wave Astronomy (CARMA) configurations with HPBWs of 0.9, 2.1, and $4.4''$ designed to explore the S1 and S2 shells at these spatial scales. Preliminary results of the D configuration observations have been presented in Harper et al. (2009). In §2 the observations and data reduction techniques are discussed and in §3 the results of the spectra and image maps are presented. Discussions and conclusions are presented in §4 and §5, respectively.

2. OBSERVATIONS AND DATA REDUCTION

The millimeter observations were made with the 15 element CARMA interferometer (Scott et al. 2004) which is located at Cedar Flat in eastern California at an elevation of 2200 m. The array consists of nine 6.1 m antennas and six 10.4 m antennas formerly from the Berkeley Illinois Maryland Association (BIMA) and the Owens Valley Radio Observatory (OVRO) arrays respectively. Table 1 summarizes the various observations which span the period 2007 May - 2009 November. The observations were carried out in the C, D, and E configurations and consist of on-source profiles of the $^{12}\text{C}^{16}\text{O}(J = 2-1)$ line which has a rest frequency of 230.538 GHz (1.3 mm). The baseline length spans over 26-370 m (C array), 11-148 m (D array), and 8.5-66 m (E array) providing beam sizes of $0.9''$, $2.1''$, and $4.4''$ respectively at 1.3 mm . The HPBW of the individual 10.4 m antennas is $\sim 32''$ at the observed frequency.

The CARMA correlator takes measurements in three separate bands, each having an upper and lower sideband. One band was set to the low resolution 468 MHz mode (15 channels of 31.25 MHz width) to observe continuum emission and was centered on the line. The other

two bands were configured with 62 MHz and 31 MHz bandwidth across 63 channels (with a resolution of 1.3 km s^{-1} and 0.65 km s^{-1} respectively) and were also centered on the line. The line was measured in the upper sideband in the C and E array and in the lower sideband in the D array.

Bandpass and phase calibration were performed using 3C120 and 0530+135. 0532+075 was used as a secondary phase calibrator to determine the quality of the phase transfer from the primary phase calibrator. The observing sequence was to integrate on the primary phase calibrator for ~ 2.5 minutes, the target for ~ 18 minutes, and the secondary phase calibrator for ~ 2.5 minutes. The cycle was repeated for each track which lasted between 1.5 hours and 5 hours. Absolute flux calibration was carried out with 0530+135 and 3C120 using the continuously updated CARMA flux catalog to obtain their flux values at each observation.

The raw data was smoothed by a Hanning filter within MIRIAD⁶ and then exported into FITS format so that it could be analyzed with the CASA⁷ data reduction package. All calibration and imaging was carried out within CASA. The image cubes were multi-scale CLEANed down to the 3σ threshold using natural weighting and were corrected for primary beam attenuation. The *multiscale* algorithm (Rich et al. 2008) within CASA was set to four unique scales; the largest corresponding to the largest structures visible in individual channel maps. Each scale was approximately set to three times smaller than the preceding scale.

Each of the three CARMA configurations sample a different range of spatial frequencies; the range of which is dependent upon the maximum and minimum baselines (b_{max} and b_{min}) of each configuration. The sources we are observing are extended and therefore it is necessary to consider the response of each CARMA configuration to this extended emission. For any array configuration, emission with angular scales of $\sim \lambda/b_{min}$ or greater is not reproduced in the maps (Taylor et al. 1999) and this scale is often used as a guide for the *resolving out scale* or *maximum scale* of an array configuration. To obtain

⁶ Multichannel Image Reconstruction, Image Analysis and Display, <http://www.atnf.csiro.au/computing/software/miriad/>
⁷ Common Astronomy Software Applications, <http://casa.nrao.edu/>

a more robust estimate of the largest angular scale that can be accurately imaged in the high spatial resolution C configuration maps we computed the visibilities of an extended emission feature (whose spatial extent was set to that of the primary beam) using CASAs simulation tool, *simdata*. This tool then produced a CLEANed image of these visibilities from which we calculated the resolving out scale to be $\sim 6''$ (i.e. $0.6\lambda/b_{min}$). Ultimately combining the data from these three configurations allows the missing short spacings from the extended C configuration to be recovered while maintaining its high spatial resolution.

3. RESULTS

Betelgeuse is a semi-regular variable and its radial velocity exhibits variability on time scales ranging from short 1.5 year periods as suggested by Stebbins & Huffer (1931) to longer 5.8 year periods (Jones, 1928). Its radial velocity amplitudes are also known to vary by at least $\pm 3 \text{ km s}^{-1}$ (Smith et al. 1989) making it difficult to determine a precise value for the stellar center-of-mass radial velocity. In this study we adopt a radial velocity of $+20.7 \text{ km s}^{-1}$ (heliocentric); a value adopted by Harper et al. (2008) and is based on the mean values of Jones (1928) and Sanford (1933). All spectra are plotted with respect to the stellar center of mass rest frame.

3.1. CO($J = 2-1$) Spectra

The spectrum for each individual configuration image cube (which are composed of all the appropriate configuration tracks listed in Table 1) along with the multi-configuration image cube can be used to obtain information on the kinematics of the S1 and S2 shells. The spectra corresponding to the C, D, and E configuration image cubes are plotted in Figure 1 for both the high (0.65 km s^{-1}) and low (1.3 km s^{-1}) spectral resolution data and were obtained by integrating all emission within a circular area of radius $4''$ centered on the source. The high and low spectral resolution modes allow two independent sets of spectra to be measured for each observation and thus provide a good check on the data quality. The high resolution spectra (channel width = 0.65 km s^{-1}) gives the best measure for shell kinematics and therefore all outflow velocities are derived from this spectra.

The E configuration image cube spectrum has a total line width of 29.2 km s^{-1} and the low spectral resolution profile contains a steep blue wing emission feature between -16.0 km s^{-1} and -11.0 km s^{-1} and a more flat-topped feature between -10.3 km s^{-1} and $+13.2 \text{ km s}^{-1}$. The steep blue wing in the high resolution profile matches the lower resolution profile well but the remainder of the profile looks more complex than the flat-topped feature seen in the lower resolution profile. The profile shape of the CO($J = 2-1$) line has been well documented by previous single dish observations (e.g. Knapp et al. 1980; Huggins 1987) and out of our three individual configuration spectra we expect the most compact E configuration spectra to resemble these single dish measurements the most due to its large resolving out scale and higher sampling rate of the inner uv-plane. This indeed turns out to be the case when we compare our three individual configuration spectra to those previous single profiles. The blue wing emission feature appears again in the D configuration spectrum at the same velocities as those in the E

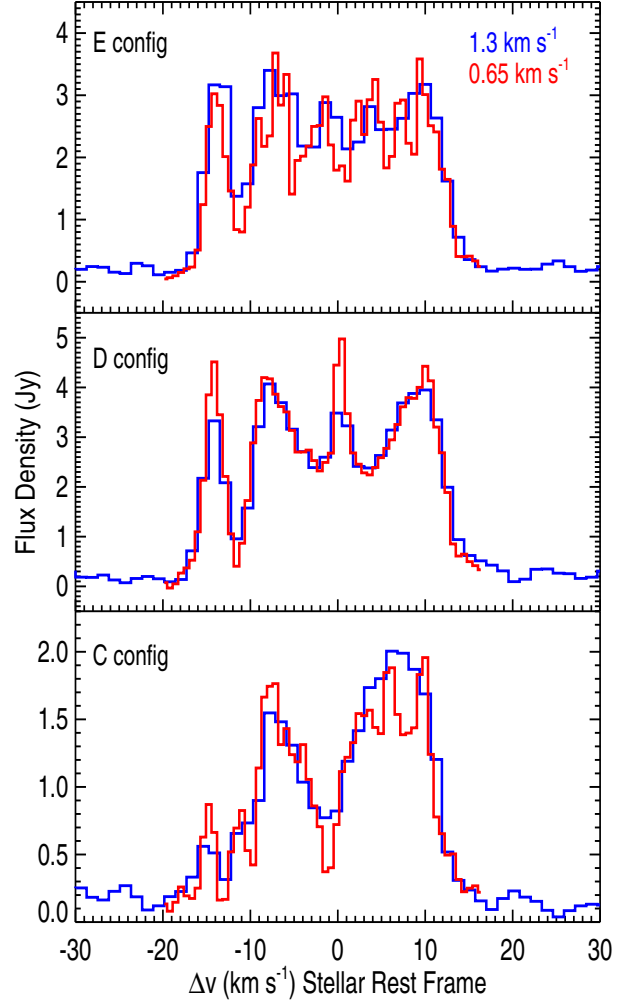


Figure 1. Spectra integrated over a radius of $4''$ for each array configuration image cube. The blueshifted emission component between -10 km s^{-1} and -16 km s^{-1} is almost resolved out in the C configuration image cube spectrum. The red and blue lines correspond to the high and low spectral resolution data respectively.

configuration spectrum but the remainder of the profile appears quite different. Between -10.3 km s^{-1} and $+13.2 \text{ km s}^{-1}$ the D configuration spectrum is dominated by a blue wing at $\sim -10 \text{ km s}^{-1}$, a red wing at $\sim +13 \text{ km s}^{-1}$ and a discrete emission feature at $\sim 0 \text{ km s}^{-1}$.

The line profile has a much lower flux in the high spatial resolution C configuration spectrum due to the small resolving out angular scale of the array. The blueshifted emission feature located between -16.0 km s^{-1} and -11.0 km s^{-1} in the E and D configuration spectra is almost completely resolved out by the extended C configuration. This component of the line has previously been associated with the outer S2 shell (Huggins 1987) and as the majority of it has been resolved out by our C configuration we expect even less contribution from the S2 shell at lower velocities still. For the redshifted line emission we again expect the majority of the S2 contribution to be resolved out, so we conclude that the majority of the emission in the C configuration spectrum emanates from the inner S1 shell. The spectrum is double peaked with the blue and redshifted wings extending to -9.0 km s^{-1}

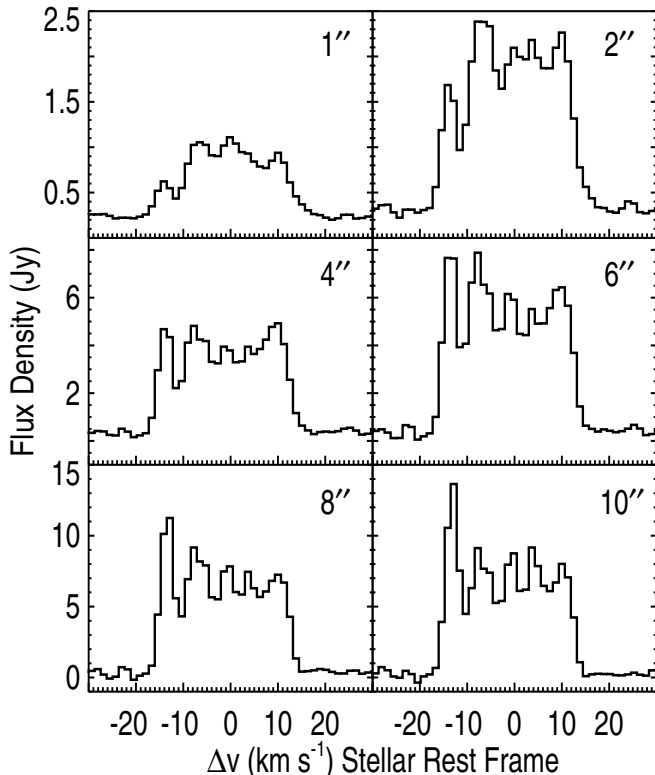


Figure 2. Spectral profiles of the low spectral resolution multi-configuration image cube for circular extraction areas of radius 1'', 2'', 4'', 6'', 8'', and 10''.

and $+10.6 \text{ km s}^{-1}$ respectively, and we define these as the outflow velocities of the S1 shell. As discussed in §2 the C configuration has a resolving out scale of $\sim 6''$ at 1.3 mm and so is not sensitive to angular scales larger than this. If the emission between -9.0 km s^{-1} and $+10.6 \text{ km s}^{-1}$ in the C configuration spectrum appeared as a flat topped profile then we could conclude that the S1 shell lies within a radius of $3''$ from the star. Clearly however, the lower absolute velocity components of this profile have been resolved out so we can conclude that the spatial extent of the S1 from the star is greater than $3''$. If we assume that the S1 shell would produce a top-hat line profile were it not for the resolving out effects of the interferometer, then its integrated line flux is $3.1 \times 10^{-19} \text{ W m}^{-2}$.

To obtain the most robust value for the S2 outflow velocities we examine the high resolution multi-configuration image cube spectrum which is composed of all tracks from all three configurations. It is worth stressing that by analyzing the multi-configuration image cube we make the crude assumption that the physical properties of all three components (i.e. α Ori, S1 shell and S2 shell) have not changed over the total observation period. The profile is found to have a total linewidth of $28.6 \pm 0.7 \text{ km s}^{-1}$, which is in close agreement with previous single dish observations of the line where values of $30.6 \pm 2.5 \text{ km s}^{-1}$ and 28.6 km s^{-1} are reported by Knapp et al. (1980) and Huggins (1987) respectively. The centroid velocity of the spectrum is -1.1 km s^{-1} ($v_{\text{lsr}} = 3.7 \pm 0.7 \text{ km s}^{-1}$) which is again in close agreement with Knapp

et al. (1980) and Huggins (1987) who report values of $3.0 \pm 2.5 \text{ km s}^{-1}$ and $3.7 \pm 0.4 \text{ km s}^{-1}$ respectively. The integrated line flux is then $1.5 \times 10^{-18} \text{ W m}^{-2}$ of which approximately 20% emanates from the S1 shell.

The outflow velocities of the S2 shell are -15.4 km s^{-1} and $+13.2 \text{ km s}^{-1}$ which again like the S1 shell are slightly asymmetric but in the opposite sense. Note that these shell outflow velocities are dependent on the adopted radial velocity of Betelgeuse. If for instance, we instead adopt a radial velocity of 21.9 km s^{-1} (Famaey et al. 2005) then the the S2 outflow velocities become even more asymmetric (-16.6 and $+12.0 \text{ km s}^{-1}$) while the S1 outflow becomes less so (-10.2 and $+9.4 \text{ km s}^{-1}$). Both shells therefore cannot have spherically symmetric outflow velocities regardless of the adopted stellar radial velocity. Adopting a mass of $18 M_{\odot}$ and a radius of $950 R_{\odot}$ (Harper et al. 2008) then the escape velocity for Betelgeuse is 85 km s^{-1} which is much greater than the S1 and S2 shell outflow velocities. This indicates that the majority of the stellar mass loss mechanism's energy goes into lifting the CO molecules out of the gravitational potential and not into their outflow velocities. These outflow velocities are greater than the adiabatic hydrogen sound speed, which, if we assume that the gas temperature is the same as the excitation temperature, are 1.7 km s^{-1} and 1 km s^{-1} for the S1 and S2 shells respectively.

The spectra in Figure 2 are taken from the low resolution multi-configuration image cube using circular extraction areas ranging in radius from $1''$ to $10''$ and demonstrates how the line profile changes over these different areas. The most striking change in the line profile is the change in appearance of the extreme blue wing. At small extraction radii where we sample the most compact emission, the feature is weak in comparison to the rest of the line but becomes more dominant as we begin to sample more of the extended emission. This indicates that even the high velocity components of the S2 shell have extended emission and this is why they are almost completely resolved out by CARMA's C configuration.

3.2. Multi-Configuration Image Cube

A subset of the blueshifted velocity channel maps of the low spectral resolution multi-configuration image cube is presented in Figure 3. The first channel map at -17.9 km s^{-1} shows just the compact unresolved continuum emission with no extended emission present. Between -16.7 km s^{-1} and -9.0 km s^{-1} we see evidence for the development of a classical shell signature for the S2 shell. We first sample the highest velocity shell components where the emission is relatively compact (i.e. between -16.7 km s^{-1} and -12.9 km s^{-1}) and then sample lower velocity components where the shell becomes a faint ring (i.e. between -11.6 km s^{-1} and -9.0 km s^{-1}). At lower velocities again, these rings disappear into the noise of the maps and possibly extend out beyond the primary beam at zero velocity when the rings should have maximum spatial extent. The emission from the channel maps between -15.3 km s^{-1} and -11.6 km s^{-1} correspond to all the emission in the extreme blue wing component of the multi-configuration image cube line profile discussed in §3.1. We can see in Figure 3 that all of this emission is greater than the C configuration resolving out scale

therefore confirming that our C configuration line profile is mainly composed of S1 shell emission. The shell formation signature of the S2 shell is also apparent in the redshifted velocity channel maps between $+7.5$ km s $^{-1}$ and $+13.8$ km s $^{-1}$ but the emission appears weaker and the rings fainter therefore indicating that the shell is inhomogeneous in density structure.

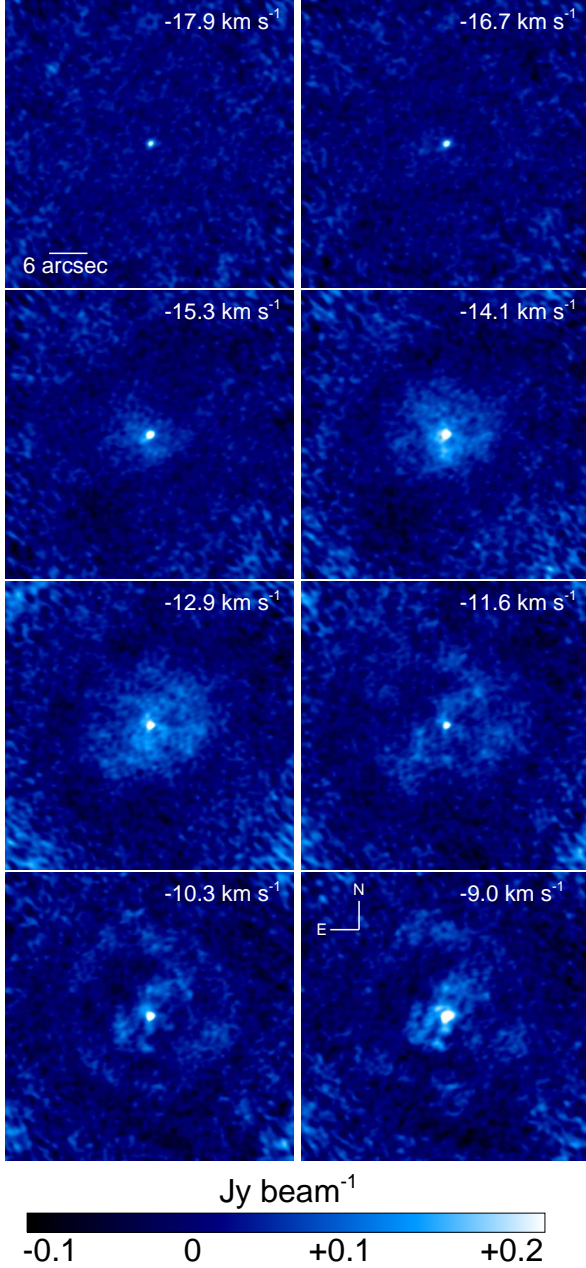


Figure 3. 8 channel maps from the multi-configuration configuration image cube. The peak emission has been cut at 0.2 Jy beam $^{-1}$ to emphasize the fainter emission. The color scale is linear and has been normalized to this maximum cutoff and minimum value of each channel. The emission at the corners of each map is a result of the primary beam correction.

The multi-configuration maps also show the central compact emission from the S1 shell at velocities between -10.3 km s $^{-1}$ and $+11.3$ km s $^{-1}$. This S1 emission can be seen in the final two maps of Figure 3 as a central

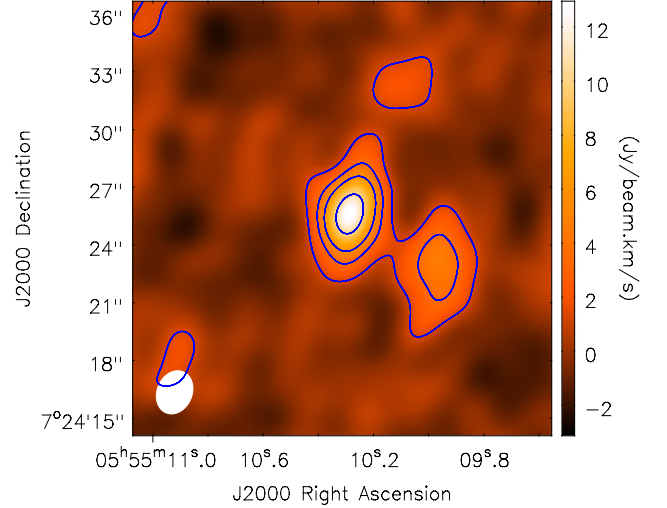


Figure 4. Integrated intensity image of the D configuration channel maps that contain the discrete second source approximately $5''$ S-W of α Ori. Contours for the integrated intensity are 1σ , 1.5σ , 2σ , and 3σ ($1\sigma = 1.3$ Jy beam $^{-1}$ km s $^{-1}$). The size of the restoring beam is shown in white in the bottom left corner.

slightly elongated emission feature surrounded by the fainter rings of the S2 shell. In the maps where both shells are present the emission from the S1 shell appears brighter than the emission from the S2 shell. The spatial extent of the S1 shell varies from channel map to channel map and we assign it a mean radius of $\sim 5''$, a value which is in good agreement with Harper et al. (2009) and Smith et al. (2009).

An additional spatially unresolved source is detected in a number of the D configuration image cube maps (both high and low spectral resolution) and has been previously documented by Harper et al. (2009). The component is present in only five continuous channels between ~ -4 km s $^{-1}$ and $+2.4$ km s $^{-1}$ and is located $\sim 5''$ S-W of α Ori as shown in Figure 4. Its peak emission lies at ~ 0 km s $^{-1}$ and here it approximately equals 60% of the source peak emission. The corresponding channel maps in the E configuration image cube show extended emission out to $8''$ in the same S-W direction. This second source does not appear in any of the C configuration channel maps and may be resolved out by this extended configuration. This discrete second source thus has the effect of adding extra emission to the corresponding multi-configuration image cube maps at the low velocities where it is present.

3.3. Determination of the Shell Radii

The spatial extent of the S1 and S2 shells around Betelgeuse was not directly determined from either the CO infrared absorption spectra of Bernat et al. (1979) or previous CO single dish radio observations (Knapp et al. 1980; Huggins 1987; Huggins et al. 1994). Our low spectral resolution multi-configuration image cube has sufficient spatial resolution and signal-to-noise to make direct estimates of the maximum radius of both shells. The outer S2 shell is not seen in the low absolute velocity channel maps where its spatial extent is maximum and either lies outside of the primary beam or is lost into the noise near the edge of the maps. We derive the maximum scale of the S2 shell by looking at the spatial scales of the S2 shell in the higher absolute velocity maps where the shell is present. If we assume that the S2 shell is spherically

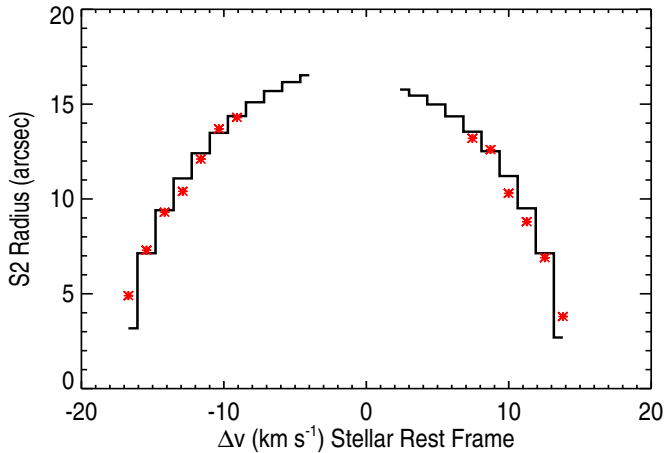


Figure 5. The derived shell radius as a function of velocity (red points) overplotted with two model shells. The blueshifted model (left) corresponds to a shell with a maximum radius of $17''$ and an outflow velocity of 17 km s^{-1} while the redshifted model (right) corresponds to a shell with a maximum radius of $16''$ and an outflow velocity of 14 km s^{-1} .

symmetric with a radius R_{s2} , and is undergoing steady expansion with velocity V_{s2} , then we can estimate the shell radius per velocity channel using the following relation:

$$r_{\text{chan}} = R_{s2} \sin \left[\cos^{-1} \left(\frac{v_{\text{chan}}}{V_{s2}} \right) \right] \quad (1)$$

where r_{chan} is the shell radius in a channel at velocity v_{chan} .

We use Equation (1) to estimate the maximum projected spatial extent of the shell which occurs at zero velocity. An estimate of the S2 shell radius per channel (r_{chan}) was found by creating annuli of increasing width around the central emission in each relevant line channel map of the multi-configuration image cube, extracting all flux within each annulus and then plotting these fluxes against distance from the star for each channel. The maximum of these resultant curves was then deemed to be the maximum radius of the S2 shell per channel. Figure 5 shows these data over-plotted with two model shells which were created using Equation (1). The blueshifted data points were best fitted by a model shell of maximum radius $17''$ and outflow velocity 17 km s^{-1} , while the redshifted data points were best fitted by a model shell of maximum radius $16''$ and outflow velocity 14 km s^{-1} . It is worth mentioning that this estimate for the spatial extent of the S2 shell is not dependent on our adopted radial velocity value for Betelgeuse and adopting a different radial velocity value would simply alter the shells outflow velocities. As the S2 shell is not present in our lowest absolute velocity map we are not able to report an estimate of the shell’s width.

In the left column of Figure 6 we investigate the intensity distribution of CO emission as a function of projected radius, R , for both the S1 and S2 shells. From our discussions in §3.1 we can assume that all line emission between $-15.4 \rightarrow -10.3 \text{ km s}^{-1}$ and $+12.4 \rightarrow +13.8 \text{ km s}^{-1}$ emanates from the S2 shell. Using the low spectral resolution multi-configuration image cube we integrate the surface brightness over these channels and find that

the intensity fall-off is proportional to R^{-1} . To investigate the S1 shell intensity distribution around $\alpha \text{ Ori}$ we integrate the surface brightness over the channels between $-9 \text{ km s}^{-1} \rightarrow +10.6 \text{ km s}^{-1}$. Although these channels contain emission from both shells, most of the S2 emission here should be extended and thus the majority of the inner emission should emanate from the S1 shell. Between $0.5''$ and $4''$ from the star the intensity is again found to be proportional to R^{-1} . Such an intensity distribution is expected for an optically thin homogeneous spherical outflow with constant velocity. Beyond $4''$ the intensity fall off is more rapid and is close to a R^{-2} distribution which may signify the end of the S1 shell.

Insight can also be gained into how the flux varies on different size scales by conducting analysis in the $u-v$ plane and plotting the visibility amplitude of $\alpha \text{ Ori}$ against $u-v$ distance. The result of this is shown in the right column of Figure 6 where the same channels corresponding to the S1 and S2 shells have been used. The data are scan and channel averaged, and have been binned to produce one data point per $k\lambda$. The result for both the S1 and S2 shell data is a steep drop-off in visibility amplitude over a relatively short $u-v$ distance, signaling that the sources are well resolved. Both sets of data can be shown to agree with an intensity drop-off of $(a^2 + R^2)^{-1/2}$, where a is an inner spatial limit. The Hankel transform of this function is $q^{-1}e^{-2\pi a q}$ (Bracewell 2000) and a scaled version of this function is shown to match the data very well in Figure 6. As the intensity of both shells is clearly proportional to R^{-1} we conclude that both outflows are optically thin and steady which is in agreement with Smith et al. (2009) (i.e. S1 shell) and Plez & Lambert (2002) (i.e. S2 shell).

An exact determination of the maximum spatial extent of the S1 shell is more difficult as we do not see the classical smooth shell formation signature for it as we sample across velocities. Instead its spatial extent varies over the channel maps with evidence of discrete clumps being present in most of these maps. The S1 shell extends out to a mean distance of $\sim 4''$ in the integrated intensity S1 map and is more extended in the S-W direction due to the presence of the second emission feature in the compact configuration data sets. The restoring beam size of $0.9''$ is not sufficient to determine whether the S1 shell is discrete or an extension of the current wind phase seen in ultraviolet spectra, e.g., (Carpenter & Robinson 1997), and cm-radio continuum interferometry (Lim et al. 1998; Harper et al. 2001).

3.4. Continuum Flux Densities

In Table 2 we show the derived continuum flux densities for each of the three configuration image cubes and also the multi-configuration image cube. The high spectral resolution ($\Delta v = 1.27 \text{ km s}^{-1}$) image cubes were just wide enough to image the CO line but were too narrow to make accurate estimates of the continuum flux density. Therefore, all continuum flux density estimates are derived from the lower spectral resolution ($\Delta v = 0.635 \text{ km s}^{-1}$) image cubes from which we were able to take accurate measurements at both sides of the line. We fitted elliptical Gaussians to ~ 20 continuum channels using CASA’s *imfit* routine allowing the flux and corresponding uncertainties to be calculated. The source was

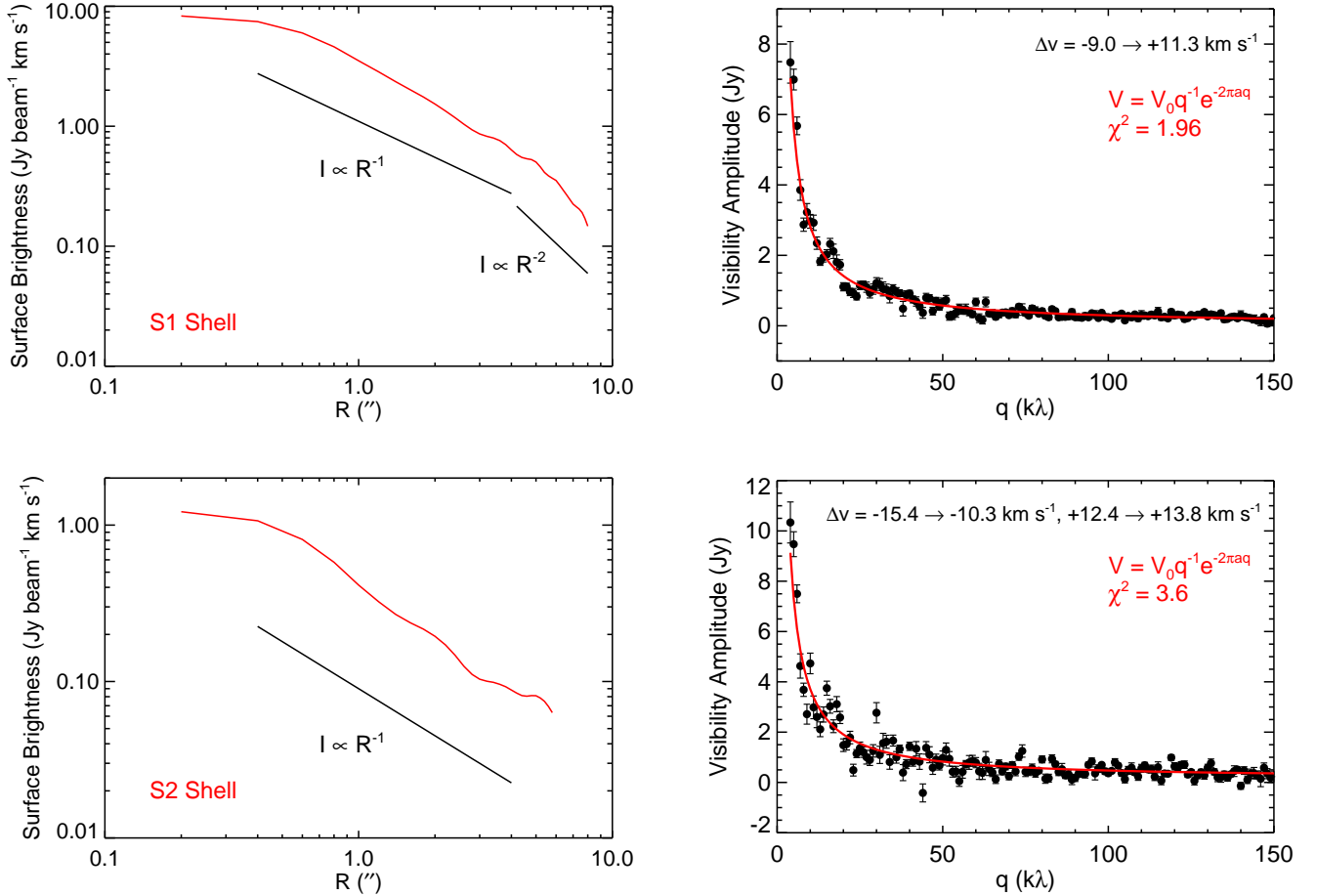


Figure 6. *Left Column:* Surface Brightness as a function of projected radius on sky, R (red line). The emission has been extracted from the low spectral resolution multi-configuration image cube and is integrated over the channels where the S1 shell is present (top) and over the channels where only the S2 shell is present (bottom). Intensity proportional to R^{-1} and R^{-2} is also shown for comparison. *Right Column:* The corresponding visibility amplitude as a function of u - v distance (q) of both shells can be modeled well by a R^{-1} fall off in intensity. The error bars represent the standard error of the mean.

unresolved in most of these continuum channels.

Betelgeuse is known to show brightness variations at many wavelengths. Goldberg (1984) reports a decrease of half a magnitude in visual brightness over a period of six years. Bookbinder et al. (1987) found stochastic 30%-40% variations in flux density at 6 cm over timescales as short as 10 days to as long as 8 months (i.e. the observational period). A more comprehensive study was carried out by Drake et al. (1992) who observed Betelgeuse with the VLA at centimeter wavelengths from 1986 to 1990 and found stochastic variability of 22%, 15%, and 21% at 6 cm, 3.6 cm, and 2 cm respectively at a variety of different timescales down to less than one month. The mm-continuum emission that we measure arises mainly from bremsstrahlung emission associated with neutral and ionized hydrogen and possibly dust emission, so it is not unreasonable to also expect variability at mm-wavelengths too. The D configuration data was acquired under adverse weather conditions and the data has the highest noise levels out of the three configurations. Its continuum emission measurement is approximately 50% greater than the C and E configuration continuum measurements which were also acquired ap-

Table 2
CARMA Continuum Fluxes

Configuration	Restoring Beam (" × ")	Flux (mJy)	Uncertainty (mJy)
C	0.96×0.76	234	18
D	2.33×1.87	389	72
E	4.93×3.84	278	40
Multi-configuration	1.05×0.84	289	21

proximately two years after the D configuration data. We believe the continuum emission derived from the multi-configuration image cube is an accurate estimation of the mm-continuum flux density over the two year period and is in reasonably good agreement with the 250 GHz flux density of Altenhoff et al. (1994) who report a value of 351 ± 25 mJy.

4. DISCUSSION

4.1. Previous CO Observations

Bernat et al. (1979) were the first to detect circumstellar absorption lines in CO by looking at the 1-0 ro-vibration line at $4.6 \mu\text{m}$. These infrared observations revealed two shells around α Ori; a warm ($T_{\text{exc}} = 200$

K) S1 shell with an expansion velocity of 9 km s^{-1} and a cooler ($T_{\text{exc}} = 70 \text{ K}$) S2 shell moving with a faster expansion velocity of 16 km s^{-1} . Knapp et al. (1980) were the first to detect emission in the $\text{CO}(J = 2-1)$ line at 1.3 mm using the 10 m millimeter-wave telescope at Owens Valley Radio Observatory but only detected one component expanding at 15 km s^{-1} . By reconciling column densities, they concluded that the shell radii derived by Bernat et al. (1979) were too large and that S2 lies at a radius of $R \leq 10''$. Since the detection by Knapp, a number of follow up observations at 1.3 mm have been carried out with various beam sizes and all spectra look remarkably similar; that is the profile has a steep extreme blue shifted emission component with the remainder of the profile looking more flat topped and containing a number of less dominant spikes. Huggins (1987) used their single dish observations (beam size $\sim 32''$) of the $\text{CO}(J = 2-1)$ line along with excitation and self-shielding models of CO to conclude that the S1 shell makes little contribution to the final emission line. They also identify the extreme blue wing of the line with the S2 shell and predict that it may extend out to a radius of $\sim 16''$. Later however, Huggins et al. (1994) compared their detected $609 \mu\text{m } ^3P_1 \rightarrow ^3P_0$ fine structure line of C I with CO data obtained with the IRAM 30m telescope (beam size $\sim 12''$) and find that the expansion velocities in both lines are essentially the same. They conclude that the radial extent of C I is $\lesssim 7''$ and both the CO and C I are formed in the inner envelope and roughly extend over the same area.

The shape of our multi-configuration line profile for extraction areas of radii $6''$ or greater are in good agreement with previous high signal to noise single dish $\text{CO}(J = 2-1)$ spectra (e.g. Huggins et al. 1994, Fig. 1.) although the emission spikes in our line profiles are more dominant. Our total line width of 28.6 km s^{-1} is in good agreement with Huggins (1987) and Huggins et al. (1994) who report line widths of 28.6 km s^{-1} and 30 km s^{-1} respectively. The extreme blue wing in both of these spectra are the dominant emission features of the line and this is also true in our multi-configuration spectra at extraction areas $\gtrsim 6''$. The IRAM 30 m telescope in Huggins et al. (1994) has a beam size of only $12''$ at 230 GHz and yet produces a similar line profile shape to Huggins (1987) who uses a larger beam size of $\sim 30''$. From this, one would expect that the majority of the blue wing emission is compact. Our multi-configuration line profiles suggest otherwise however, and show a continuous increase in the blue wing emission as we take larger extraction regions out to $10''$. The multi-configuration maps also show a faint ring structure forming at $\sim 11.6 \text{ km s}^{-1}$ and expanding further out as we sample across the channels. This ring emission is fainter than the higher velocity compact emission so we see a drop in flux density in our spectra at the point where these rings form. Therefore, the steepness of the extreme blue wing in our multi-configuration spectrum does not actually mean that we are resolving the S2 shell but merely that there is more CO emitting at higher velocities than at lower.

The line profiles of higher CO rotational transitions for Betelgeuse have been published in Kemper et al. (2003) and De Beck et al. (2010). De Beck et al. (2010) present high spectral resolution (0.3125 MHz) line profiles for the

$\text{CO}(J = 2-1)$, ($J = 3-2$), and ($J = 4-3$) transitions that were obtained with the James Clerk Maxwell Telescope (JCMT). For the $\text{CO}(J = 2-1)$ transition the JCMT has a HPBW of $\sim 20''$ and the profile appears similar to our multi-configuration profile over the same flux density extraction area (i.e. Figure 2), with the extreme blue wing component being the dominant feature in both. This feature, which is emission from the S2 shell becomes a less dominant component of the line profile at the higher $\text{CO}(J = 3-2)$ and $\text{CO}(J = 4-3)$ transitions where the JCMT has a HPBW of $\sim 13''$ and $8''$ respectively, and does not capture all of the S2 emission which is shown in Figure 3 to be extended at these velocities. We expect this trend in the change of the profile shape to continue at higher rotational transitions again where the HPBW would be smaller thus capturing even less of the S2 emission. Also the probability of these high rotational states being occupied would become increasingly less (assuming an S2 excitation temperature of 70 K) and therefore the profile would become dominated by emission from the S1 shell with its higher excitation temperature ($\sim 200 \text{ K}$).

The CO $4.6 \mu\text{m}$ vibration-rotational lines have been observed with the Phoenix spectrograph (Hinkle et al. 1998) by Ryde et al. (1999) and Smith et al. (2009) on the 2.1 m telescope at Kitt Peak and on the 8.1 m Gemini South telescope respectively. By assuming a Boltzmann population distribution for the ground rotational levels of CO Ryde et al. (1999) derived a mean excitation temperature of 38_{-5}^{+6} K along the line of sight at a projected distance of $4''$ north of Betelgeuse with a slit length of $50''$. Our CARMA data suggests that the S1 shell extends out beyond this but Ryde et al.'s temperature is not in agreement with either of the line-of-sight S1 or S2 excitation temperatures of $200_{-10}^{+50} \text{ K}$ and $70 \pm 10 \text{ K}$ derived by Bernat et al. (1979). This discrepancy may indicate the excitation is quite non-uniform. Smith et al. (2009) did not derive an excitation temperatures but used their $4.6 \mu\text{m}$ spectra to reveal extended resonantly scattered CO emission out to $\sim 3 - 5''$ in good agreement with our mean S1 radial value. They observe emission over a velocity range of 30 km s^{-1} but two distinct shells are not detected. Mild ($\sim 20\%$) density inhomogeneities are reported but overall, their observations are consistent with a spherical, optically thin and steady wind.

4.2. K I 7699 \AA spectra

The S2 shell was first identified in high resolution K I and Na I absorption spectra by Goldberg et al. (1975) and subsequently re-observed multiple times over the next couple of years (Goldberg 1979). It is interesting to compare these line-of-sight velocities with those from the CARMA emission spectra obtained at similar spectral resolutions.

We have obtained K I 7698.98 \AA spectra using the cross-dispersed echelle spectrometers on the Harlan J. Smith 107 inch (2.7m) reflector at McDonald Observatory. With two pixels per resolution element a $R = \lambda/\Delta\lambda = 200,000$ and a $R = 500,000$ spectrum were obtained in 2007 March 25 and April 13, universal time, respectively. The spectra were wavelength calibrated with ThAr lamp lines and the lower resolution spectrum was checked by fitting six symmetric terrestrial O_2 lines in the same order using wavelengths from Babcock & Herzberg

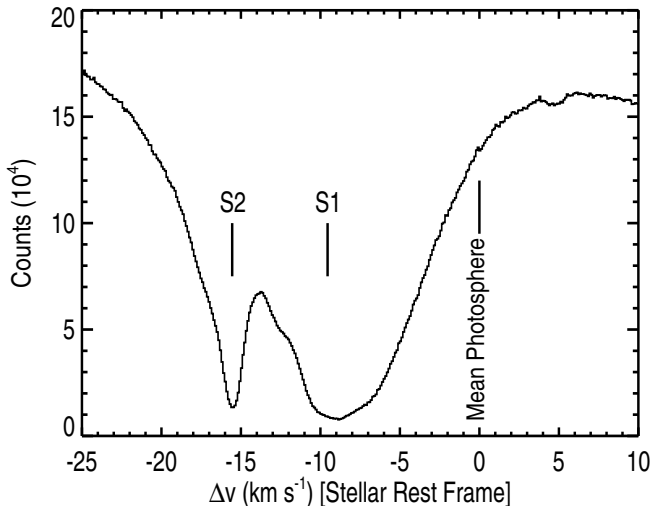


Figure 7. The K I 7698.98 Å profile ($R=500,000$) for Betelgeuse obtained on April 13th 2007. The S2 shell outflow velocity is found to be 15.6 km s^{-1} (using a $V_{\text{rad}} = +20.7 \text{ km s}^{-1}$), slightly lower than Plez & Lambert’s (2002) value of $18 \pm 2 \text{ km s}^{-1}$.

(1948). The O_2 lines confirmed the $R=200,000$ calibration was good to better than 0.1 km s^{-1} . Upon cross-correlating the low and high resolution spectrum the high resolution spectrum appeared redshifted by 0.60 km s^{-1} , i.e., one resolution element, for which we do not have an explanation except to note that a similar offset has been reported by Welty et al. (1994). We use the cross-correlation to define the wavelength calibration of the $R = 500,000$ spectrum and we adopt a systematic error of 0.2 km s^{-1} .

The high-resolution spectrum is shown in Figure 7 in the adopted stellar centre-of-mass rest frame ($V_{\text{rad}} = +20.7 \text{ km s}^{-1}$). The S2 feature is deep, well separated from the S1 feature, and very well represented by a simple absorption model with hyperfine splitting. We adopt the K I 7698.9645 Å line parameters compiled in Morton (2003)⁸ and find a heliocentric S2 absorption velocity of $+5.1 \text{ km s}^{-1}$ and a most probable line-of-sight turbulent velocity of 0.60 km s^{-1} . There is also a slight inflection in the underlying profile at $+3.6 \text{ km s}^{-1}$ (heliocentric) which may represent structure in the underlying photospheric profile or additional absorption in which case it has ~ 0.1 the column density of S2. The S2 absorption minimum can be compared to those obtained by Goldberg (1979, Fig 7) who measured values between 1975 and 1978 of 4.2 ± 0.2 and $5.0 \pm 0.2 \text{ km s}^{-1}$ and these differences may result from changes caused by radial velocity changes in the underlying photospheric spectrum. Bernat et al.’s 1979 CO IR absorption observations reveal S2 heliocentric velocities of $+4.94 \pm 0.30 \text{ km s}^{-1}$ (1979 Mar 6) and $+4.60 \pm 0.04 \text{ km s}^{-1}$ (1979 Apr 14) with turbulent velocities of 4 and 1 km s^{-1} for the S1 and S2 features, respectively.

In terms of the center-of-mass radial velocity of the star our K I feature implies an outflow velocity of

$+15.6 \text{ km s}^{-1}$. The blue edge of our CARMA multi-configuration CO profile is estimated to be $+15.4 \text{ km s}^{-1}$ which suggests a dynamical association with the CO S2 shell and very close agreement with Bernat et al.’s (1979) CO absorption velocities listed above. Plez & Lambert (2002) have also estimated the radius and velocity of the suspected K I S2 shell using $R = 110,000$ resolution long slit spectra. They found a geometrically thin shell ($1''$) with velocity of $V_{S2} = 18 \pm 2 \text{ km s}^{-1}$ with a radius of $55''$ which is much larger than the field of view of the CARMA spectra. Their long slit spectra show several smaller partial shells but it is not simple to directly associate the CO emission feature with one or more of these shells especially given the uncertainty in the ionization balances of CO and K I.

5. CONCLUSIONS

The two distinct velocity components seen by Bernat et al. (1979) in CO absorption against the stellar spectrum at $4.6 \mu\text{m}$ have both been detected at 230 GHz for the first time. The first velocity component known as S1 has an expansion velocity of 9 km s^{-1} (Bernat et al. 1979) and is detected in our high spectral resolution C configuration profile with the same blueshifted velocity (i.e. 9.0 km s^{-1}) and with a larger redshifted outflow velocity of 10.6 km s^{-1} . The extended CARMA C configuration has a resolving out scale of $\sim 6''$ and thus resolves out almost all of the S2 emission leaving us with an approximate spectrum for the S1 shell. An extreme blue wing of the CO spectrum appears in the D and E configuration spectra which we associate with the S2 shell. The high spectral resolution multi-configuration spectrum is used to determine S2 outflow velocities of -15.4 km s^{-1} and $+13.2 \text{ km s}^{-1}$ which is in good agreement with our K I 7699 Å line of sight S2 velocity and that reported by Bernat et al. (1979).

Our derived S1 radius is in good agreement with the the Phoenix measurements of Smith et al. (2009) and our high spatial resolution multi-configuration maps provide the first direct measurements on the spatial extent of the S2 shell, which we derive to have a radius of $17''$; a value that higher than most previous estimates. Previous single dish observations of the CO line with small HPBW’s do not show the classical resolved signature of high emission at large absolute velocities and low emission at low absolute velocities for two main reasons. Firstly, the S1 shell is still unresolved in these single dish observations and thus contributes emission and at the lower absolute velocities. As well as this, the multi-configuration CARMA maps show that the S2 shell emission is brighter in the higher absolute velocity maps than at lower absolute velocities and so when the emission from the fainter rings is neglected (i.e. when they are resolved), the overall line profile does not change significantly. Assuming a mean constant outflow velocity of 14.3 km s^{-1} and 9.8 km s^{-1} for the S2 and S1 shell respectively then their ages are $\sim 1100 \text{ yr}$ and $\sim 470 \text{ yr}$.

Support for CARMA construction was derived from the states of California, Illinois, and Maryland, the James S. McDonnell Foundation, the Gordon and Betty Moore Foundation, the Kenneth T. and Eileen L. Norris Foundation, the University of Chicago, the Associates

⁸ Note that this wavelength is 0.44 km s^{-1} less than that adopted in the Goldberg studies.

of the California Institute of Technology, and the National Science Foundation. Ongoing CARMA development and operations are supported by the National Science Foundation under a cooperative agreement, and by the CARMA partner universities.

Based [in part] on observations made with the NASA/DLR Stratospheric Observatory for Infrared Astronomy. SOFIA Science Mission Operations are conducted jointly by the Universities Space Research Association, Inc., under NASA contract NAS2-97001, and the Deutsches SOFIA Institut under DLR contract 50 OK 0901. GREAT is a development by the MPI fr Radioastronomie and the KOSMA/ Universitt zu Kln, in cooperation with the MPI fr Sonnensystemforschung and the DLR Institut fr Planetenforschung.

Facilities: CARMA, McDonald Observatory and SOFIA.

REFERENCES

- Airapetian, V. S., Ofman, L., Robinson, R. D., Carpenter, K., & Davila, J. 2000, *ApJ*, 528, 965
- Altenhoff, W. J., Thum, C., & Wendker, H. J. 1994, *A&A*, 281, 161
- Babcock, H. D., & Herzberg, L. 1948, *ApJ*, 108, 167
- Bernat, A. P., Hall, D. N. B., Hinkle, K. H., & Ridgway, S. T. 1979, *ApJ*, 233, L135
- Bookbinder, J. A., Stencel, R. E., Drake, S. A., Simon, T., Linsky, J. L., & Florkowski, D. 1987, in *Lecture Notes in Physics*, Berlin Springer Verlag, Vol. 291, Cool Stars, Stellar Systems and the Sun, ed. J. L. Linsky & R. E. Stencel, 337
- Bracewell, R. N. 2000, *The Fourier transform and its applications*, ed. Bracewell, R. N.
- Carpenter, K. G., & Robinson, R. D. 1997, *ApJ*, 479, 970
- Danchi, W. C., Bester, M., Degiacomi, C. G., Greenhill, L. J., & Townes, C. H. 1994, *AJ*, 107, 1469
- De Beck, E., Decin, L., de Koter, A., Justtanont, K., Verhoelst, T., Kemper, F., & Menten, K. M. 2010, *A&A*, 523, A18
- Drake, S. A., Bookbinder, J. A., Florkowski, D. R., Linsky, J. L., Simon, T., & Stencel, R. E. 1992, in *Astronomical Society of the Pacific Conference Series*, Vol. 26, Cool Stars, Stellar Systems, and the Sun, ed. M. S. Giampapa & J. A. Bookbinder, 455
- Famaey, B., Jorissen, A., Luri, X., Mayor, M., Udry, S., Dejonghe, H., & Turon, C. 2005, *A&A*, 430, 165
- Glassgold, A. E., & Huggins, P. J. 1986, *ApJ*, 306, 605
- Goldberg, L. 1979, *QJRAS*, 20, 361
- . 1984, *PASP*, 96, 366
- Goldberg, L., Ramsey, L., Testerman, L., & Carbon, D. 1975, *ApJ*, 199, 427
- Harper, G. M., Brown, A., & Guinan, E. F. 2008, *AJ*, 135, 1430
- Harper, G. M., Brown, A., & Lim, J. 2001, *ApJ*, 551, 1073
- Harper, G. M., Carpenter, K. G., Ryde, N., Smith, N., Brown, J., Brown, A., & Hinkle, K. H. 2009, in *American Institute of Physics Conference Series*, Vol. 1094, American Institute of Physics Conference Series, ed. E. Stempels, 868–871
- Hartmann, L., & Avrett, E. H. 1984, *ApJ*, 284, 238
- Hinkle, K. H., Cuberly, R. W., Gaughan, N. A., Heynssens, J. B., Joyce, R. R., Ridgway, S. T., Schmitt, P., & Simmons, J. E. 1998, in *Society of Photo-Optical Instrumentation Engineers (SPIE) Conference Series*, Vol. 3354, Society of Photo-Optical Instrumentation Engineers (SPIE) Conference Series, ed. A. M. Fowler, 810–821
- Huggins, P. J. 1987, *ApJ*, 313, 400
- Huggins, P. J., Bachiller, R., Cox, P., & Forveille, T. 1994, *ApJ*, 424, L127
- Kemper, F., Stark, R., Justtanont, K., de Koter, A., Tielens, A. G. G. M., Waters, L. B. F. M., Cami, J., & Dijkstra, C. 2003, *A&A*, 407, 609
- Knapp, G. R., & Morris, M. 1985, *ApJ*, 292, 640
- Knapp, G. R., Phillips, T. G., & Huggins, P. J. 1980, *ApJ*, 242, L25+
- Lambert, D. L., & Vanden Bout, P. A. 1978, *ApJ*, 221, 854
- Lim, J., Carilli, C. L., White, S. M., Beasley, A. J., & Marson, R. G. 1998, *Nature*, 392, 575
- Morton, D. C. 2003, *ApJS*, 149, 205
- Plez, B., & Lambert, D. L. 2002, *A&A*, 386, 1009
- Rich, J. W., de Blok, W. J. G., Cornwell, T. J., Brinks, E., Walter, F., Bagetakos, I., & Kennicutt, Jr., R. C. 2008, *AJ*, 136, 2897
- Ryde, N., Gustafsson, B., Hinkle, K. H., Eriksson, K., Lambert, D. L., & Olofsson, H. 1999, *A&A*, 347, L35
- Sanford, R. F. 1933, *Contributions from the Mount Wilson Observatory / Carnegie Institution of Washington*, 464, 1
- Scott, S. L., et al. 2004, in *Astronomical Society of the Pacific Conference Series*, Vol. 314, Astronomical Data Analysis Software and Systems (ADASS) XIII, ed. F. Ochsenbein, M. G. Allen, & D. Egret, 768–+
- Smith, M. A., Patten, B. M., & Goldberg, L. 1989, *AJ*, 98, 2233
- Smith, N., Hinkle, K. H., & Ryde, N. 2009, *AJ*, 137, 3558
- Stebbins, J., & Huffer, C. M. 1931, *Publications of the Washburn Observatory*, 15, 178
- Taylor, G. B., Carilli, C. L., & Perley, R. A., eds. 1999, *Astronomical Society of the Pacific Conference Series*, Vol. 180, Synthesis Imaging in Radio Astronomy II
- Welty, D. E., Hobbs, L. M., & Kulkarni, V. P. 1994, *ApJ*, 436, 152
- Weymann, R. 1962, *ApJ*, 136, 844

APPENDIX

SOFIA OBSERVATIONS

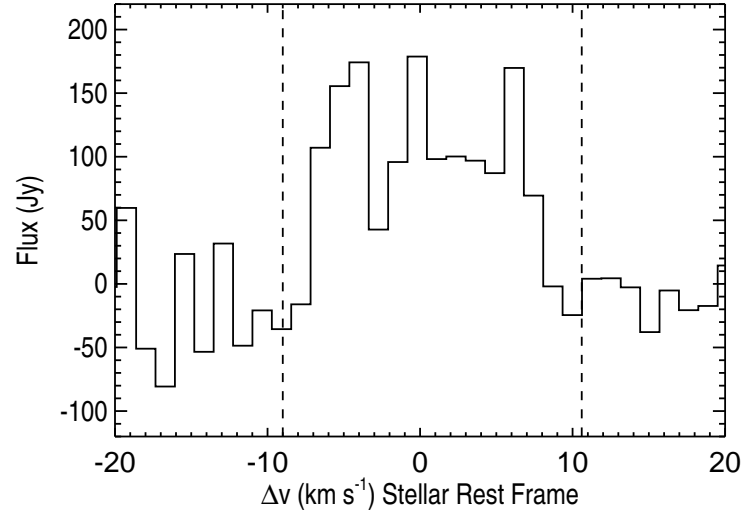


Figure 8.